

# Online camera-pose-free stereo endoscopic tissue deformation recovery with tissue-invariant vision-biomechanics consistency

Jiahe Chen<sup>a</sup>, Naoki Tomii<sup>a</sup>, Ichiro Sakuma<sup>a</sup>, Etsuko Kobayashi<sup>a</sup>

<sup>a</sup>*School of Engineering, The University of Tokyo, Tokyo, 113-8656, Japan*

---

## Abstract

Tissue deformation recovery based on stereo endoscopic images is crucial for tool-tissue interaction analysis and benefits surgical navigation and autonomous soft tissue manipulation. Previous research suffers from the problems raised from camera motion, occlusion, large tissue deformation, lack of tissue-specific biomechanical priors, and reliance on offline processing. Unlike previous studies where the tissue geometry and deformation are represented by 3D points and displacements, the proposed method models tissue geometry as the 3D point and derivative map and tissue deformation as the 3D displacement and local deformation map. For a single surface point, 6 parameters are used to describe its rigid motion and 3 parameters for its local deformation. The method is formulated under the camera-centric setting, where all motions are regarded as the scene motion with respect to the camera. Inter-frame alignment is realized by optimizing the inter-frame deformation, making it unnecessary to estimate camera pose. The concept of the canonical map is introduced to optimize tissue geometry and deformation in an online approach. Quantitative and qualitative experiments were conducted using *in vivo* and *ex vivo* laparoscopic datasets. With the inputs of depth and optical flow, the method stably models tissue geometry and deformation even when the tissue is partially occluded or moving outside the field of view. Results show that the 3D reconstruction accuracy in the non-occluded and occluded areas reaches  $0.37 \pm 0.27$  mm and  $0.39 \pm 0.21$  mm in terms of surface distance, respectively. The method can also estimate surface strain distribution during various manipulations as an extra modality for mechanical-based analysis.

**Keywords:** Tissue deformation recovery, Tissue tracking, Nonrigid

## 1. Introduction

Tissue deformation is the change in its 3D structure and connectivity in time. In surgery, tissue deformation is typically caused by tool-tissue interaction and cardio-respiratory pulsation. Analyzing tissue deformation benefits many downstream tasks, such as surgical navigation (Schneider et al., 2021), surgical simulation (Zhu et al., 2022), analyzing tool-tissue interaction (Chen et al., 2023, 2024b), manipulation risk assessment (Yamamoto et al., 2023), and autonomous soft tissue manipulation (Hu et al., 2024; Chen et al., 2024a).

Deformation recovery is to estimate and quantify the dynamic change of tissue shape, which is typically 4D data involving spatiotemporal information. Most of the existing deformation recovery methods are based on the stereo vision system, such as the binocular endoscopic (Chavarrias Solano et al., 2025), the binocular laparoscopic (Chen et al., 2023), or the binocular microscopic camera (Giannarou et al., 2016). There are typically two subtasks of deformation recovery: 3D reconstruction and inter-frame alignment. 3D reconstruction is to acquire tissue 3D structure, while inter-frame alignment is to establish time domain connection.

Difficulties in tissue deformation recovery are mostly derived from its non-rigid nature. The motion of a rigid object can be completely represented by a 6-degree of freedom (DoF) transformation, while the deformation of a non-rigid object has infinite DoF. Inter-frame alignment of a rigid scene is almost equal to finding the true camera pose in different frames, while the estimated camera pose is less reliable in a deformable scene and less useful for the alignment. On the other hand, the common interference during surgery also hinders accurate deformation estimation. The interference resulted by occlusion, camera motion, specular reflection, lowly textured surface, and surface discontinuity are the common causes of 3D reconstruction and tracking failure.

In most of the recent vision-based deformation recovery methods, tissue deformation is usually represented by the displacement field (Giannarou et al., 2016; Chen et al., 2024b; Wang et al., 2022), which merely has 3-DoF. However, surface rotation and inner-surface stretching are not modeled, which are up to 12-DoF and are necessary to represent 3D surface deformation from the perspective of continuum mechanics. Therefore, we

reformulate the commonly used definition of tissue deformation in a vision-based approach by adding the additional parameters to represent pointwise rotation and stretching. We also propose a camera-centric setting to get rid of the dependence on camera pose. Based on all these prerequisites, we proposed an online method to concurrently optimize tissue geometry and deformation leveraging the tissue-invariant vision-biomechanics consistency constraint.

The concept of camera-centric deformation recovery in this article was first introduced in our conference paper (Chen et al., 2024b), but it is the first time that the detailed methodology was reported. Besides, this article overcomes the limitation in our old method and is not a simple extension of it.

### 1.1. Related work

*3D reconstruction.* 3D scene reconstruction is the basis of tissue deformation recovery, which provides tissue 3D structure as a depth map, point cloud, or mesh. Typical sensors for vision-based 3D reconstruction are either monocular or stereo (binocular) cameras. Monocular image-based 3D reconstruction in a single frame is an ill-posed problem, as a single 2D frame loses the 3D information. Only relative depth can be estimated (Budd and Vercauteren, 2024). Scaling factors need to be estimated to convert the relative depth to the absolute one (Chavarrias Solano et al., 2025; Wei et al., 2024), which remains challenging and the accuracy of which is typically lower than the stereo-based approach. Stereo image-based 3D reconstruction is typically formulated as a stereo matching problem. Given a single pair of the left and right frames, it is theoretically sufficient to recover a 3D structure (Xia et al., 2022; Psychogyios et al., 2022; Bardozzo et al., 2022). However, due to occlusion, smoking, lowly textured surfaces, duplicated textures, and specular reflection problems, mismatches always occur, leading to erroneous reconstructed results.

*Inter-frame alignment.* Inter-frame alignment is necessary for continuous tissue deformation recovery. Tissue structures reconstructed from different frames may lie in different camera coordinates due to camera motion. Camera pose is used to represent camera orientation and position under the reference coordinate and can be used to transform frame data into the same coordinate. Camera pose estimation in robotic surgery can be realized by leveraging

robot kinematics (Li et al., 2020; Yoshimura et al., 2021). However, kinematics data typically suffer from the accumulative error in joint encoders and are inaccurate without careful calibration. Image-based camera pose estimation is another solution (Luo et al., 2023; Hayoz et al., 2023). However, camera pose estimation in a deformable scene is an ill-posed problem, as it is hardly possible to decouple camera and scene motion without identifying reliable rigid landmarks. Moreover, camera pose has only 6 DoF and is insufficient to describe the infinite DoF non-rigid deformation. Therefore, even if the camera pose can be perfectly estimated, it barely helps in tissue deformation recovery. To represent the infinite-DoF deformation, the displacement field is commonly used, which can describe the pointwise motion. Currently, the displacement field can be represented either implicitly or explicitly. An implicit displacement field is implemented using the neural field (Wang et al., 2022; Zha et al., 2023; Yang et al., 2024; Guo et al., 2024). However, implicit displacement field is typically trained in an offline approach, and there is currently no evidence that it can achieve high tracking accuracy. Explicit displacement field is also named as scene flow. It can be estimated leveraging the 3D reconstruction and 2D tracking information (Schmidt et al., 2024; Stoyanov, 2012; Giannarou et al., 2016; Chen et al., 2023, 2024b). Scene flow can easily represent the inter-frame motion of data points and thus is a good candidate for inter-frame alignment. However, vision-derived scene flow inherits the error of 3D reconstruction and 2D tracking and is typically rough and noisy.

*Simultaneous reconstruction and alignment.* The tasks of 3D reconstruction and inter-frame alignment are often treated as one task. Under such problem settings, the most famous methods are the simultaneous localization and mapping (SLAM) and structure from motion (SfM) families (Gómez-Rodríguez et al., 2021; Lamarca et al., 2021; Ozyoruk et al., 2021; Chen et al., 2018; Widya et al., 2019; Shao et al., 2022; Recasens et al., 2021; Shan et al., 2024). These methods concurrently optimize camera pose and reconstruct 3D scenes and typically have long-term stability. Although these endoscopic SLAM and SfM methods are adapted to deformable scenes by adding some flexibility in modeling structure deformation, they still cannot handle large deformation and are not robust to tool-induced occlusion. More importantly, these methods focus more on reconstructing panoramic scenes while paying little attention to continuous point tracking in the time domain.



*Biomechanics-driven deformation estimation.* Biomechanical properties, such as stiffness and elasticity, are used in modeling the tissue dynamic behavior. Once the tissue-specific biomechanical property is available, a deformation model can be established to estimate and predict tissue deformation under tool-tissue interaction. Such technique is commonly used in surgical simulation (Scheikl et al., 2023; Zhu et al., 2022) and also appears to be used in processing the real deformable object videos (Haouchine et al., 2018, 2015). However, tissue-specific and patient-specific tissue biomechanical properties are usually unavailable in real surgery, limiting the use of the biomechanics-driven method. Additionally, estimating tissue property from endoscopic images becomes possible by leveraging vision-derived deformation (Liang et al., 2024; Xu et al., 2022); however, this turns out to be a chicken-and-egg problem.

### 1.2. Contributions

The proposed method overcomes the limitations of previous vision-based deformation recovery methods and contributes to the following points:

*Deformation and geometry representation.* Besides the previously used time-variant displacement field (3-DoF) and 3D surface points (3-DoF) for representing tissue deformation and geometry, the proposed method additionally uses the time-variant local deformation field (6-DoF) and surface differential geometry (6-DoF) to better represent tissue’s dynamics.

*Camera-centric and camera-pose-free.* The method neither requires the camera pose as input, estimates it, nor uses it in reconstruction. The method treats all movement as the scene movement with respect to the camera. In other words, this is a static-camera-dynamic-scene setting that is naturally suitable for dynamically deformable scene, which is different from the frequently used moving-camera-static-scene setting in the field of SLAM and others.

*Tissue-invariant.* The method does not rely on tissue-specific biomechanical priors.

*Occlusion robust.* Deformation and structure in the occluded area can still be recovered.

*Online.* The method works in an online manner and does not involve offline optimization. Historical and the latest data are maintained under the proposed canonical mechanism.

## 2. Preliminaries

### 2.1. Camera-pose-free scene reconstruction

Camera pose represents the orientation and position of a camera with respect to a reference coordinate. Camera pose is commonly estimated by SfM techniques (Widya et al., 2019; Schonberger and Frahm, 2016) or acquired by robot kinematics (Li et al., 2020; Yoshimura et al., 2021) and is useful in scene 3D reconstruction. The term “camera-pose-free” in previous methods (Guo et al., 2024; Recasens et al., 2021; Gómez-Rodríguez et al., 2021) often refers to the unnecessary of the camera pose as input. However, these methods still attempt to estimate the camera pose inside their algorithms, or in other words, the camera pose is still crucial and indispensable for scene reconstruction. Different from the previous one, the meanings of “camera-pose-free” in this article are twofold: 1. the camera pose is unnecessary as input; 2. the camera pose is totally not considered in the problem formulation nor used in reconstruction.

Accurately acquiring camera pose in surgical intervention remains challenging. Robot kinematics-based methods (Li et al., 2020; Yoshimura et al., 2021) suffer from accumulated errors from joint encoders and calibration. On the other hand, image-based camera pose estimation (Hayoz et al., 2023) in the deforming scene is extremely difficult, as it is an ill-posed problem to decouple the motion of the object and the camera. The inaccuracy in camera pose may hinder the stability and reliability of tissue reconstruction. Moreover, even an error-free camera pose<sup>1</sup> barely helps in tissue deformation recovery without pointwise tracking or registration.

Therefore, in this article, we do not attempt to estimate the camera pose or decouple the motion of the scene and the camera. Instead, eliminating the camera pose gives us a novel camera-centric problem setting. In the frame-by-frame deformation recovery process, the geometry and deformation are always represented within the latest camera coordinates. All the inter-frame motion is regarded as the scene motion with respect to the camera.

---

<sup>1</sup>In the case where the camera is fixed, we can say there is no error in camera pose.

## 2.2. Tissue surface deformation representation

Previously, tissue deformation is often represented by various displacement fields, such as the neural field (Pumarola et al., 2021; Wang et al., 2022; Zha et al., 2023), pointwise displacements (Chen et al., 2023; Stoyanov, 2012; Giannarou et al., 2016), or displacement maps (Chen et al., 2024b). These displacement fields describe the 3D displacements of the tissue surface points between frames or relative to a reference frame. However, they cannot directly tell the deformation within a given region on the tissue surface, since the 3D displacement  $(\Delta x, \Delta y, \Delta z) \in \mathbb{R}^3$ , as a 3-DoF descriptor, is not enough to describe 3D deformation.

In continuum mechanics (Spencer, 2004), we need a 12-DoF descriptor to represent the 3D deformation for a volume, as shown in Fig. 1, where 6-DoF are used to represent the rigid motion and the other 6-DoF are for the local deformation. The 12-DoF 3D deformation descriptor can be described as  $\mathbf{d} \in \{SE(3), \varepsilon^6\}$ , where  $SE(3)$  is the Lie group representing the homogeneous transformation of the rigid motion, and  $\varepsilon^6$  represents the strain, including three normal strains and three shear strains. Since the polar decomposition in continuum mechanics can directly get the stretch rather than the strain, for convenience, we use stretch instead of strain in the following text, such that the 3D deformation is as  $\mathbf{d} \in \{SE(3), \xi^6\}$ , where  $\xi^6$  represents the stretch. One can transform stretch to strain without effort. For a 3D surface, as shown in Fig. 1, the representation of 3D deformation can be simplified to  $\mathbf{d} \in \{SE(3), \xi^3\}$ .

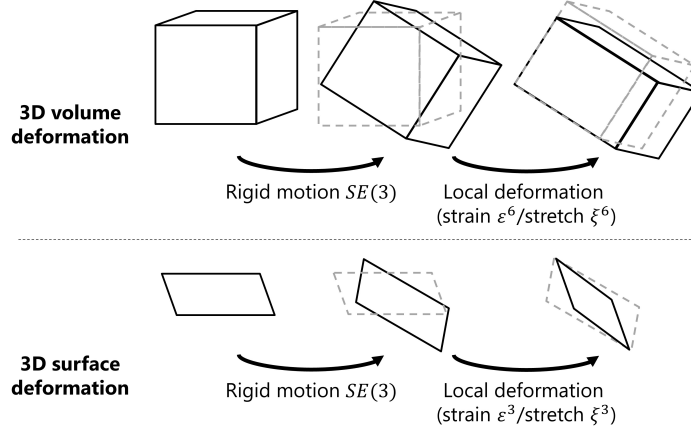


Figure 1: The representation of deformation in the 3D space.

The description of local deformation is rotation-variant; for convenience, we define  $\mathbb{D} = (r^3, \xi^3)$  as a local deformation descriptor, where  $r^3 = SO(3)$  is the special orthogonal group representing 3D rotation and  $\xi^3$  is the inner-surface stretch. Finally, the 3D surface deformation is as  $\mathbf{d} \in \{\mathbb{F}, \mathbb{D}\}$ , where the  $\mathbb{F} = \mathbb{R}^3$  stands for 3D displacement. We claim this as a sufficient representation for 3D surface deformation.

### 2.3. Problem setting

#### 2.3.1. Prerequisites and assumptions

1. The proposed method relies on two measurements: the 3D scene structure and 2D tracking, typically the 3D point cloud and the 2D optical flow map. These measurements are always noisy. Noises may come from specular reflection, duplicated texture, low-textured regions, self-occlusion, tool-induced occlusion, camera motion, and tissue sudden breaking.
2. The mask generated from instrument segmentation is accurate or can at least cover the whole region of the instrument in the image.
3. The method is online. Only the latest and the second-latest frame data are involved in optimization.
4. The camera can be either fixed or moving, while the camera pose is always unnecessary and will not be estimated.
5. Tissue surfaces may temporarily or permanently appear or disappear due to camera motion and surgical manipulation and can also be cut through in the case of dissection.
6. Vision-biomechanics consistency assumption: inter-frame deformation is limited, and the deformation between neighboring local surfaces is similar.

#### 2.3.2. Objectives

Given the measured 3D scene structure and 2D tracking, we want to estimate the geometry and the deformation  $\mathbf{d} \in \{\mathbb{F}, \mathbb{D}\}$  of the tissue surface. Tissue geometry and deformation can be estimated even if the region is currently occluded by surgical instruments or is located outside the field of view.

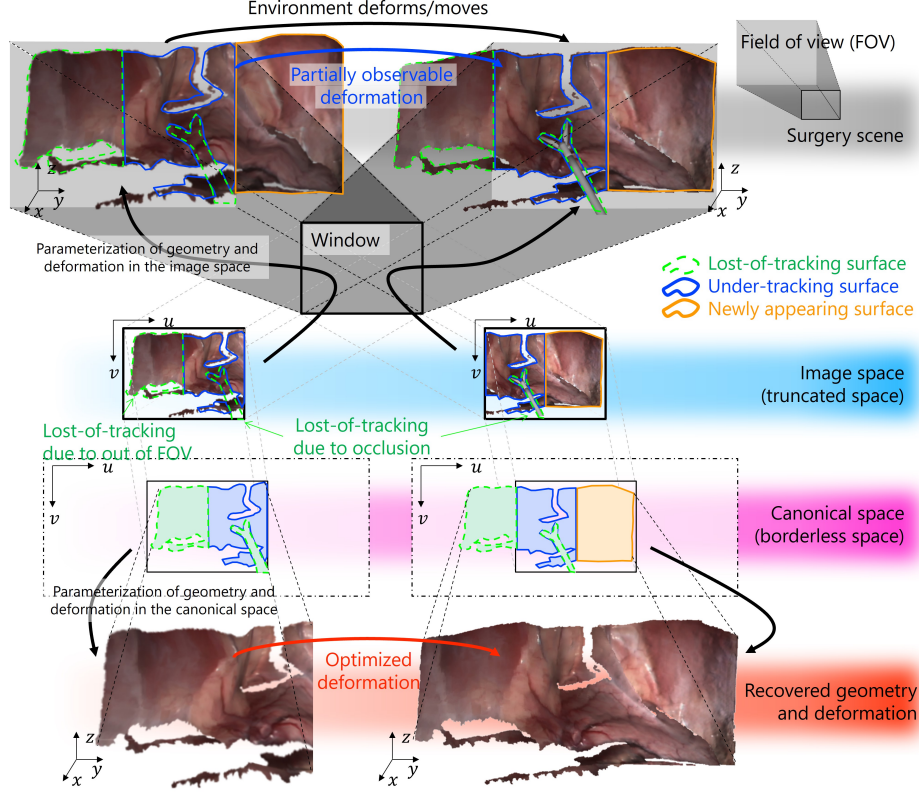


Figure 2: Schematic of the proposed method, showing how the method works within one iteration.

### 3. Methods

#### 3.1. Overview

We present a vision-based tissue deformation recovery method with robustness to occlusion and camera motion under a camera-centric problem setting. Tissue geometry and deformation used in the method are mapped in either the canonical space or the image space, as shown in Fig. 2. The method assumes that the tissue deformation is partially observable and optimizes the geometry and deformation with tissue connectivity and vision-biomechanics consistency. Such optimization is performed in an online approach: when a new frame comes, the frame map together with the last recovered map gets involved in the optimization. The newly appearing area in the new frame will then be fused into the optimized canonical map. Such design brings us

the two major benefits: 1. the method can handle camera motion while not being influenced by camera pose estimation error; 2. the method is robust to occlusion and can always reveal the latest observation, such as the instant change in tissue texture and shape.

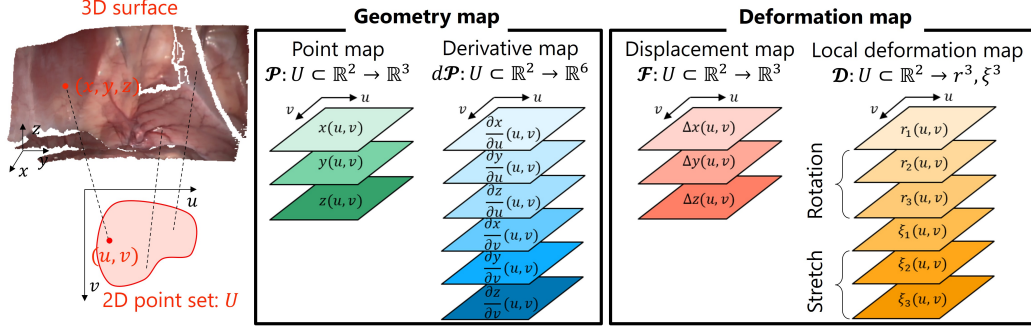


Figure 3: The parameterization of a 3D surface and the corresponding geometry and deformation map.

### 3.2. Parameterization of 3D surface geometry and deformation

In this article, a parameterization is a map to describe 3D geometry and deformation using 2D parameters. Parameterization helps to reduce the dimensional complexity required for describing the 3D geometry and deformation and to establish connectivity relationships among data points, which is crucial in optimization.

Given a 3D surface geometry  $S = \{(x, y, z) | x, y, z \in \mathbb{R}\}$ , such as a 3D point cloud or a mesh, a commonly used method for parameterization is to project the 3D points/vertices onto a 2D plane, resulting in a set of 2D points  $U = \{(u, v) | u, v \in \mathbb{R}\}$ , which creates a 2D-3D map  $\mathcal{P}: U \rightarrow S$ , as shown in Fig. 3. If the 3D geometry is provided as a depth/disparity image (Lipson et al., 2021; Xia et al., 2022), or a 3D point map (Chen et al., 2024b), then naturally these can be regarded as a parameterization of 3D geometry. To avoid sharp edges and discontinuity in the structure, we parameterize only the subset of the 3D surface, such that  $\mathcal{P}$  is a homeomorphism and differentiable. Accordingly, we can define the derivative of  $\mathcal{P}$  as:

$$d\mathcal{P}(u, v) = \begin{pmatrix} \frac{\partial x}{\partial u} & \frac{\partial y}{\partial u} & \frac{\partial z}{\partial u} & \frac{\partial x}{\partial v} & \frac{\partial y}{\partial v} & \frac{\partial z}{\partial v} \end{pmatrix} \quad (1)$$

which form the tangent plane of the surface  $S$  at the point  $\mathbf{p} = \mathcal{P}(u, v)$ , representing local surface orientation and inclination (do Carmo, 2016), as shown in Fig. 4. In this article, both the 3D point map  $\mathcal{P}$  and its derivative map  $d\mathcal{P}$  are used to represent surface geometry, so called geometry map, as shown in Fig. 3.

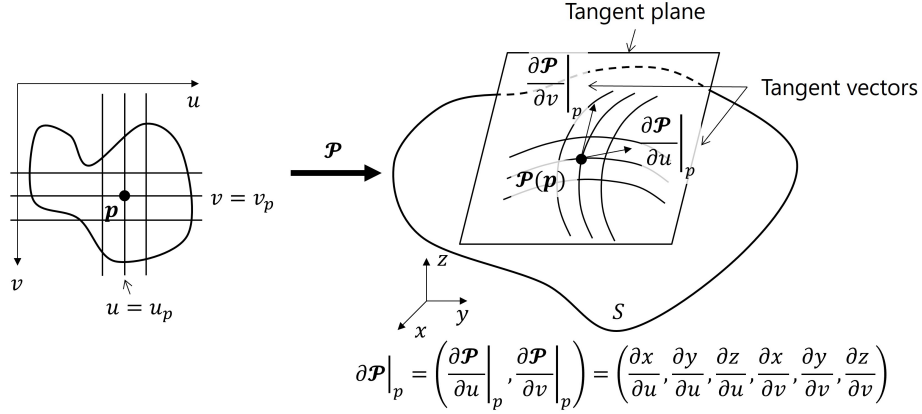


Figure 4: The geometric meaning of the derivative of a 3D point map in the sense of differential geometry.

The deformation in this article is defined as  $\mathbf{d} \in \{\mathbb{F}, \mathbb{D}\}$ , which contains the 3D displacement  $\mathbb{F}$  and the local deformation  $\mathbb{D}$ . 3D displacement can be directly obtained from the measurement. Let's first ignore occlusion and assume each data point has a 3D displacement, such that we have a displacement map  $\mathcal{F} : U \rightarrow \mathbb{F}$ . After displacement, a map to describe the new point locations is  $\mathcal{P}' = \mathcal{P} + \mathcal{F}$ . Consequently, the derivative of  $\mathcal{P}'$  is  $d\mathcal{P}'$ . We can then calculate the local deformation  $\mathbf{d} \in \mathbb{D}$  containing surface rotation and inner-surface stretching. Finally, the parameterized tissue local deformation is as  $\mathcal{D} : U \rightarrow \mathbb{D}$ . The 3D displacement map  $\mathcal{F}$  and the local deformation map  $\mathcal{D}$  together are named deformation map, as shown in Fig. 3.

### 3.3. Image space and canonical space

Maps from the 2D space to higher dimensional space have been established via parameterization. Intuitively, the 2D space will be the image space, which is a truncated 2D space due to the physical limitation of the field of view (FoV). However, image space throws away data once the object moves outside the FoV. To address this problem, a canonical space is proposed for

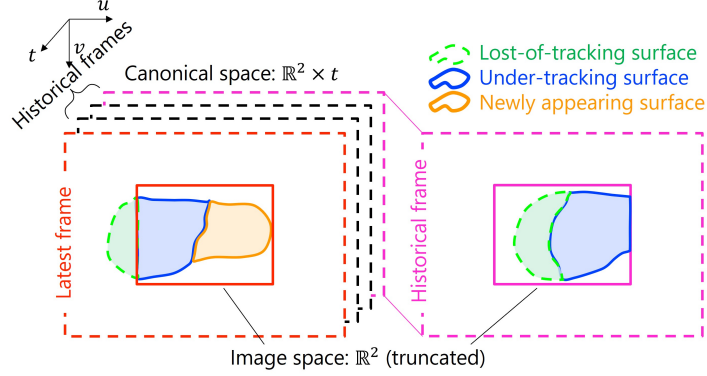


Figure 5: Illustration of the canonical space and the image space. The canonical space is a borderless 2D space with time domain and keeps both the historical and the latest data, while the image space is a truncated 2D space, such that information in the image space may get lost.

maintaining both the historical and the latest observed data. The canonical space is a borderless 2D space with a time dimension where all maps of the finalized reconstruction are defined. As a camera-centric setting, the per-frame image space is always aligned at the center of the canonical space, as shown in Fig. 5. The data in the image space always reveal the latest observation, while the data in the canonical keeps the latest optimized as well as the historical data.

### 3.4. Notation and conventions

For clarification, this section explains the naming rules of the variables used in the algorithm. Most of the variables are maps from the parameter space, including the image space and the canonical space, to the higher dimensional space representing various modeled quantities, including 3D point positions, surface derivatives, 3D displacement (scene flow), 2D displacement (optical flow), local deformation, and texture. As shown in Table 1, depending on whether these maps are defined in the image or the canonical parameter spaces, their subscripts are “I” or “C”, respectively. To distinguish maps at different frames, additional subscript representing time is added. For example,  $\mathcal{P}_I|_{t+1}$  represents a point map defined in the image space at time  $t+1$ , while  $\mathcal{F}_C|_t$  represents a displacement map defined in the canonical space at time  $t$ . Note that  $t$  refers to a discretized measurement frame index rather



than physical time.

Table 1: Notation of maps

n-D space \ 2D parameter space		Image $U_I = \{(u, v)   u, v \in \mathbb{R}\}$	Canonical $U_C = \{(u, v)   u, v \in \mathbb{R}\}$
3D point	$\mathbb{R}^3$	$\mathcal{P}_I : U_I \rightarrow \mathbb{R}^3$	$\mathcal{P}_C : U_C \rightarrow \mathbb{R}^3$
Surface derivative (local geometry)	$\mathbb{R}^6$	$d\mathcal{P}_I : U_I \rightarrow \mathbb{R}^6$	$d\mathcal{P}_C : U_C \rightarrow \mathbb{R}^6$
3D displacement (scene flow)	$\mathbb{F} = \mathbb{R}^3$	$\mathcal{F}_I : U_I \rightarrow \mathbb{F}$	$\mathcal{F}_C : U_C \rightarrow \mathbb{F}$
Local deformation (rotation and stretching)	$\mathbb{D} = (r^3, \xi^3)$	$\mathcal{D}_I : U_I \rightarrow \mathbb{D}$	$\mathcal{D}_C : U_C \rightarrow \mathbb{D}$
2D displacement (optical flow)	$\mathbb{R}^2$	$\mathcal{O}_I : U_I \rightarrow \mathbb{R}^2$	$\mathcal{O}_C : U_C \rightarrow \mathbb{R}^2$
Texture	$RGB$	$\mathcal{C}_I : U_I \rightarrow RGB$	$\mathcal{C}_C : U_C \rightarrow RGB$

### 3.5. Algorithm overview

The proposed modeling algorithm works in an online approach. In each iteration, inter-frame data get involved in the calculation. Let's say the current frame is at time  $t + 1$  and the last frame is at time  $t$ . The algorithm in each iteration involves three steps: 1). optimization of the canonical deformation; 2). reparameterization; and 3). map fusion. The algorithm is illustrated in Fig. 6.

*Inputs.* We have the measurement of tissue geometry at each frame via 3D reconstruction, which are represented by maps defined in the image space as  $\mathcal{P}_I|_t$ ,  $d\mathcal{P}_I|_t$ ,  $\mathcal{P}_I|_{t+1}$ , and  $d\mathcal{P}_I|_{t+1}$ . Based on these inter-frame geometry measurement, we can measure the 3D deformation maps  $\mathcal{F}_I|_t$  and  $\mathcal{D}_I|_t$ . Previously modeled canonical geometry maps  $\mathcal{P}_C|_t$  and  $d\mathcal{P}_C|_t$  are also used as inputs. If the frame at  $t$  is the initial frame, the canonical geometry maps are initialized to be the same as  $\mathcal{P}_I|_t$  and  $d\mathcal{P}_I|_t$ . Note that the raw inputs of these maps contain the parts not belonging to the tissue but to the surgical instrument, which are removed out using surgical instrument segmentation.

*Outputs.* The final outputs of the algorithm are the canonical deformation maps<sup>2</sup>  $\mathcal{F}_C|_t$  and  $\mathcal{D}_C|_t$  and the canonical geometry maps  $\mathcal{P}_C|_{t+1}$  and  $d\mathcal{P}_C|_{t+1}$ .

<sup>2</sup>These are "forward deformation". They describe how the data points at  $t$  deform.

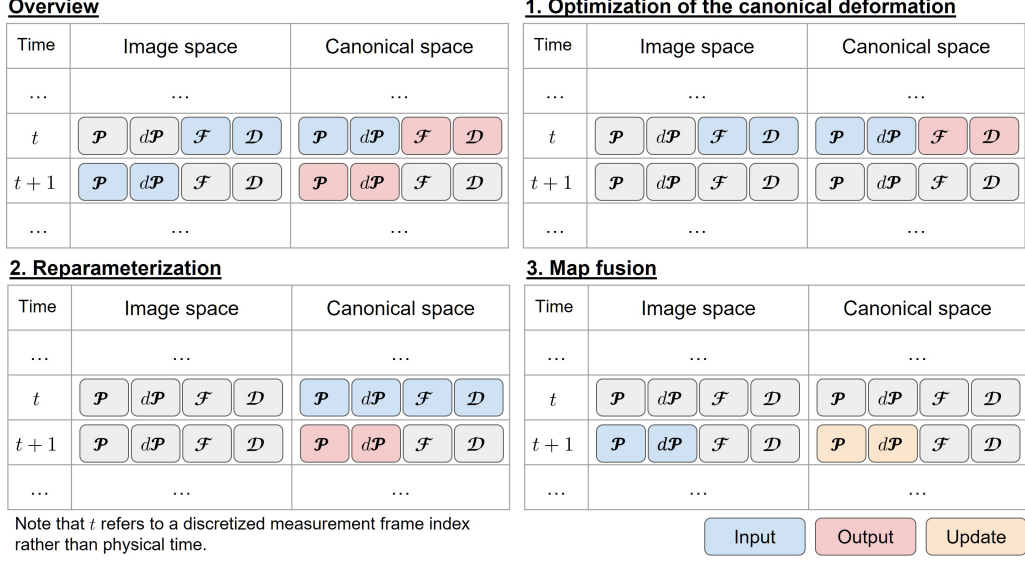


Figure 6: Illustration of the deformation recovery algorithm per iteration.

### 3.6. Optimization of the canonical deformation

The desired output deformation maps  $\mathcal{F}_C|_t$  and  $\mathcal{D}_C|_t$  are defined on the canonical parameter set  $U_C|_t$ . Parts of the canonical deformation maps can be initialized using the input deformation maps  $\mathcal{F}_I|_t$  and  $\mathcal{D}_I|_t$  defined on the image parameter set  $U_I|_t$ . The initializable deformation is also called the observable deformation. However, since  $U_C|_t \neq U_I|_t$  due to tracking loss,  $\mathcal{F}_C|_t$  and  $\mathcal{D}_C|_t$  is not fully defined in  $U_C|_t$ . Therefore, to acquire a fully defined canonical deformation map, we design an optimization method leveraging the observable deformation. In the following sections, we first introduce tissue-invariant vision-biomechanics consistency and then show how it helps outlier detection and deformation optimization. An overview of the algorithm is shown in Algorithm 1.

#### 3.6.1. Tissue-invariant vision-biomechanics consistency

Vision-derived measurement of deformation ( $\mathcal{F}_I|_t, \mathcal{D}_I|_t$ ) is typically noisy, sensitive to occlusion, and limited in the field of view. The noises in visual measurement may come from various sources, such as specular highlight, occlusion, and camera motion (Chen et al., 2024b; Zhang et al., 2023). It is difficult to quantify all the error sources and eliminate the corresponding noises specifically. This urges us to propose a more universal denoising solution.

---

**Algorithm 1:** Optimization of the canonical deformation

---

**input** :  $\mathcal{F}_I|_t : U_I|_t \rightarrow \mathbb{F}$  - the 3D displacement map defined in the image space;  
 $\mathcal{D}_I|_t : U_I|_t \rightarrow \mathbb{D}$  - the local deformation map defined in the image space;  
 $\mathcal{P}_C|_t : U_C|_t \rightarrow \mathbb{R}^3$  - the 3D point map defined in the canonical space;  
 $d\mathcal{P}_C|_t : U_C|_t \rightarrow \mathbb{R}^6$  - the derivative map defined in the canonical space  
**output**:  $\hat{\mathcal{F}}_C|_t : U_C|_t \rightarrow \mathbb{F}$  - the estimated 3D displacement map defined in the canonical space;  
 $\hat{\mathcal{D}}_C|_t : U_C|_t \rightarrow \mathbb{D}$  - the estimated local deformation map defined in the canonical space

- 1 Detect the outlier and separate  $U_C|_t$  into the inlier set  $U_{C,i}|_t$  and the outlier set  $U_{C,o}|_t$ ;
- 2 Optimize  $\mathcal{D}_C|_t$  using  $\mathcal{D}_I|_t$ ; the estimated result is  $\hat{\mathcal{D}}_C|_t$ ;
- 3 Deform the local geometry  $d\mathcal{P}_C|_t$  using  $\hat{\mathcal{D}}_C|_t$  and get  $d\hat{\mathcal{P}}'_C|_t$ ;
- 4 **if** Surgical instrument pose is available **then**
- 5     Optimize  $\mathcal{F}_C|_t$  using  $\mathcal{F}_I|_t$ ,  $\mathcal{P}_C|_t$ ,  $d\hat{\mathcal{P}}'_C|_t$  subject to the instrument pose constraint; the estimated result is  $\hat{\mathcal{F}}_C|_t$ ;
- 6 **else**
- 7     Optimize  $\mathcal{F}_C|_t$  using  $\mathcal{F}_I|_t$ ,  $\mathcal{P}_C|_t$ , and  $d\hat{\mathcal{P}}'_C|_t$ ; the estimated result is  $\hat{\mathcal{F}}_C|_t$ .
- 8 **end**

---

Fortunately, what's for sure is that the tissue deformation we observed in surgical videos has to be consistent with the biomechanism. Although many biomechanical properties are tissue-specific (Haouchine et al., 2018; Scheikl et al., 2023), making them hardly possible to be applied to universal intra-operative cases, we still manage to summarize some that are tissue-invariant. To ensure the vision-derived deformation is biomechanically reasonable, we introduce the following assumptions.

*Limitation of the inter-frame strain.* Given the truth that a common frame-per-second (FPS) of the surgical video is higher than 30, we can assume that the deformation, or strain, between frames should be trivial. Empirically, the principal strain should not be smaller than  $-0.1$  nor larger than  $0.1$ . This gives us a very rough yet efficient constraint to limit the inter-frame deformation. Local disturbance caused by various error sources typically results in a relatively large strain and thus can be detected.

*Similarity of neighboring deformation.* Given two adjacent locations,  $\mathbf{p}_1$  and  $\mathbf{p}_2$ , on the surface, we assume their corresponding local deformation,  $\mathbf{d}_1$  and  $\mathbf{d}_2$ , are similar. In this article, the local deformation is represented as  $\mathbf{d} \in \mathbb{D}$  and can be divided into rotation  $\mathbf{r} \in r^3 = SO(3)$  and stretch  $\boldsymbol{\xi} \in \xi^3$ . Therefore, we have  $\mathbf{r}_1 \approx \mathbf{r}_2$  and  $\boldsymbol{\xi}_1 \approx \boldsymbol{\xi}_2$ . This assumption is based on the connectivity of surface geometry and the continuity of deformation and regards local tissue biomechanical properties to be the same.

### 3.6.2. Outlier detection

Outliers in the canonical deformation map result in inaccuracy and instability and thus need to be filtered out before moving on to the optimization. Each data point  $(u, v)$  in the canonical parameter set  $U_C|_t$  is either an inlier or an outlier. The unobservable data points  $(u, v) \in U_C|_t \setminus U_I|_t$ , including the occluded ones and the outside-field-of-view ones, are regarded as outliers. The tool-induced occlusion can be indicated by the mask derived from instrument segmentation (Wang et al., 2022; Psychogyios et al., 2022; Wang et al., 2025). Besides, there also exist outliers in the observable data points  $(u, v) \in U_C|_t \cap U_I|_t$  that do not satisfy the vision-biomechanics consistency. For example, if the principal strain component in  $\mathcal{D}_I|_t(u, v)$ ,  $(u, v) \in U_C|_t \cap U_I|_t$  exceeds the inter-frame strain limitation as discussed in section 3.6.1, the data point is marked as an outlier. Finally, data points in  $U_C|_t$  are separated into the inlier  $U_{C,i}|_t$  and the outlier  $U_{C,o}|_t$  sets. For the data points in the inlier set, their corresponding deformation should be similar to the observation, as:

$$\mathcal{F}_C|_t(u, v) \approx \mathcal{F}_I|_t(u, v), \mathcal{D}_C|_t(u, v) \approx \mathcal{D}_I|_t(u, v), \text{ for } (u, v) \in U_{C,i}|_t \quad (2)$$

### 3.6.3. Optimization of deformation

The optimization of canonical deformation maps is performed for the local deformation map  $\mathcal{D}_C|_t$  first and then for the displacement map  $\mathcal{F}_C|_t$ . This is because the regularization term in the optimization function for  $\mathcal{F}_C|_t$  involves the local geometry term that must be updated by  $\mathcal{D}_C|_t$ .

*Local deformation.* According to the assumptions of vision-biomechanics consistency in section 3.6.1, the local deformation of neighboring regions should be similar, as:

$$\mathcal{D}_C|_t(\mathbf{p}_i) \approx \mathcal{D}_C|_t(\mathbf{p}_j); i \neq j; \mathbf{p}_i, \mathbf{p}_j \in U_C|_t \quad (3)$$

where  $\mathbf{p}_i$  and  $\mathbf{p}_j$  are adjacent. To keep the consistency with the observation as in Eq.(2), the optimization function for the local deformation map in the least square sense is:

$$\int_{\mathbf{p} \in U_{C,i}|_t} \|\mathcal{D}_C|_t(\mathbf{p}) - \mathcal{D}|_t(\mathbf{p})\|^2 + \alpha \int_{\mathbf{p}_i, \mathbf{p}_j \in U_C|_t, i \neq j} \|\mathcal{D}_C|_t(\mathbf{p}_i) - \mathcal{D}_C|_t(\mathbf{p}_j)\|^2 \quad (4)$$

where Eq.(3) is used as a regularization term ( $\mathbf{p}_i$  and  $\mathbf{p}_j$  are adjacent), and  $\alpha$  is a scalar weight that may depends on the camera resolution and the

physical scale of the tissue. To guarantee smoothness, we empirically fix  $\alpha$  to 200 in all our experiments. The estimated local deformation map  $\hat{\mathcal{D}}_C|_t$  can be found that minimizes Eq.(4) using linear solvers.

*Displacement.* The displacement map is not directly optimized. Instead, we optimize the deformed 3D point map. The reason is because after optimizing the local deformation, we can update the local geometry and use it as a regularization term that preserves local smoothness and continuity. As mentioned in section 3.2, we can deform the local geometry  $d\mathcal{P}_C|_t$  using  $\hat{\mathcal{D}}_C|_t$  and acquire  $d\hat{\mathcal{P}}'_C|_t$ , which is the estimated local geometry after deformation. If the estimated local deformation is correct, we will have:

$$d\mathcal{P}'_C|_t(\mathbf{p}) \approx d\hat{\mathcal{P}}'_C|_t(\mathbf{p}); \mathbf{p} \in U_C|_t \quad (5)$$

where  $d\mathcal{P}'_C|_t$  is the derivative of the deformed 3D point map. To keep the consistency with the observation as in Eq.(2), the optimization function for the 3D point map in the least square sense is:

$$\int_{\mathbf{p} \in U_{C,i}|_t} \|\mathcal{P}'_C|_t(\mathbf{p}) - \mathcal{P}_C|_t(\mathbf{p}) - \mathcal{F}_I|_t(\mathbf{p})\|^2 + \int_{\mathbf{p} \in U_C|_t} \|d\mathcal{P}'_C|_t(\mathbf{p}) - d\hat{\mathcal{P}}'_C|_t(\mathbf{p})\|^2 \quad (6)$$

where Eq.(5) is used as a regularization term. The optimized 3D point map  $\hat{\mathcal{P}}'_C|_t$  is found that minimizes Eq.(6). After that, it is trivial to calculate the displacement map by  $\hat{\mathcal{F}}_C|_t = \hat{\mathcal{P}}'_C|_t - \mathcal{P}_C|_t$ .

*Instrument pose-constrained optimization.* If the pose of the surgical instrument is available, it can be used to constrain the optimization of geometry to improve the accuracy, especially in the contact area between the instrument tip and the tissue, as introduced in our previous work (Chen et al., 2024a). To leverage instrument pose constraints, we have to introduce the assumption that the target tissue is always under the instrument, that is:  $z' > z_t$ , where  $z'$  is the depth component in  $\mathcal{P}'_C|_t(u, v) = (x', y', z')$  and  $z_t$  is the tool depth of its bottom surface. Such a constraint can be applied to Eq.(6) to guide the optimization.

### 3.7. Reparameterization

After the optimization of canonical deformation, now we estimate the optimized canonical deformation maps ( $\hat{\mathcal{F}}_C|_t$  and  $\hat{\mathcal{D}}_C|_t$ ) and use them to deform the canonical geometry maps ( $\mathcal{P}_C|_t : U_C|_t \rightarrow \mathcal{S}_C|_t$  and  $d\mathcal{P}_C|_t$  :

$U_C|_t \rightarrow d\mathcal{S}_C|_t$ ), where  $\mathcal{S}_C|_t = \{\mathbb{R}^3\}$  and  $\mathcal{S}_C|_t = \{\mathbb{R}^6\}$  stand for the geometry sets. The deformed canonical geometry maps are  $\hat{\mathcal{P}}'_C|_t : U_C|_t \rightarrow \hat{\mathcal{S}}'_C|_t$  and  $d\hat{\mathcal{P}}'_C|_t : U_C|_t \rightarrow d\hat{\mathcal{S}}'_C|_t$ , where  $\hat{\mathcal{S}}'_C|_t = \{\mathbb{R}^3\}$  and  $\hat{\mathcal{S}}'_C|_t = \{\mathbb{R}^6\}$  stand for the deformed geometry sets. However, all these maps are still defined in the canonical parameter set  $U_C|_t$  rather than  $U_C|_{t+1}$ . In fact,  $U_C|_{t+1}$  is still undefined so far. To move on to the latest frame at  $t + 1$ , it is necessary to align the canonical space to the latest image space, that is, to establish maps defined in  $U_C|_{t+1}$ . Therefore, we parameterize the deformed geometry ( $\hat{\mathcal{S}}'_C|_t$  and  $d\hat{\mathcal{S}}'_C|_t$ ) following the same methods in section 3.2 and then acquire the 3D point map  $\hat{\mathcal{P}}'_C|_{t+1} : \hat{U}'_C|_{t+1} \rightarrow \hat{\mathcal{S}}'_C|_{t+1}$  and its derivative map  $d\hat{\mathcal{P}}'_C|_{t+1} : \hat{U}'_C|_{t+1} \rightarrow d\hat{\mathcal{S}}'_C|_{t+1}$ . The texture map is bound to the point map and can be updated accordingly. The procedure is also shown in Algorithm 2. Note that  $\hat{\mathcal{S}}'_C|_{t+1}$  is a subset of  $\hat{\mathcal{S}}'_C|_t$  as not all geometry can be parameterized in the projection-based approach<sup>3</sup>.

---

**Algorithm 2:** Reparameterization

---

- input** :  $\hat{\mathcal{F}}_C|_t : U_C|_t \rightarrow \mathbb{F}$  - the estimated 3D displacement map defined in the canonical space;  
 $\hat{\mathcal{D}}_C|_t : U_C|_t \rightarrow \mathbb{D}$  - the estimated local deformation map defined in the image space;  
 $\mathcal{P}_C|_t : U_C|_t \rightarrow \mathbb{R}^3$  - the 3D point map defined in the canonical space at  $t$ ;  
 $d\mathcal{P}_C|_t : U_C|_t \rightarrow \mathbb{R}^6$  - the derivative map defined in the canonical space at  $t$ ;  
 $\mathcal{C}_C|_t : U_C|_t \rightarrow RGB$  - the texture map defined in the canonical space at  $t$
- output**:  $\hat{\mathcal{P}}'_C|_{t+1} : \hat{U}'_C|_{t+1} \rightarrow \mathbb{R}^3$  - the reparameterized 3D point map defined in the canonical space at  $t + 1$ ;  
 $d\hat{\mathcal{P}}'_C|_{t+1} : \hat{U}'_C|_{t+1} \rightarrow \mathbb{R}^6$  - the reparameterized derivative map defined in the canonical space at  $t + 1$ ;  
 $\hat{\mathcal{C}}'_C|_{t+1} : \hat{U}'_C|_{t+1} \rightarrow RGB$  - the reparameterized texture map defined in the canonical space at  $t + 1$
- 1 Deform the geometry maps  $\mathcal{P}_C|_t$  and  $d\mathcal{P}_C|_t$  using  $\hat{\mathcal{F}}_C|_t$  and  $\hat{\mathcal{D}}_C|_t$ , and get  $\hat{\mathcal{P}}'_C|_t$  and  $d\hat{\mathcal{P}}'_C|_t$ , respectively;
  - 2 Parameterize  $\hat{\mathcal{P}}'_C|_t$  and  $d\hat{\mathcal{P}}'_C|_t$  and get  $\hat{\mathcal{P}}'_C|_{t+1}$  and  $d\hat{\mathcal{P}}'_C|_{t+1}$ , respectively;
  - 3 Update the bound texture from  $\mathcal{C}_C|_t$  to  $\hat{\mathcal{C}}'_C|_{t+1}$
- 

### 3.8. Map fusion

Although we have deformed the canonical geometry map and aligned it to the latest frame, most of the data points in the map are inherited from the previous frames, which means that it cannot represent the newly appearing

---

<sup>3</sup>The geometry that is self-folding or located at the back of the camera cannot be parameterized.

data. Fusion is to merge the newly appearing map defined in the latest image parameter set  $U_I|_{t+1}$  to the one defined in the canonical parameter set  $U_C|_{t+1}$  as shown in Algorithm 3. Finally, both the updated historical data and the newly appearing data are merged together in the canonical space and will be involved in the optimization in the next iteration, as shown in Fig. 6.

---

**Algorithm 3:** Map fusion

---

**input** :  $\mathcal{P}_I|_{t+1} : U_I|_{t+1} \rightarrow \mathbb{R}^3$  - the 3D point map defined in the image space;  
 $d\mathcal{P}_I|_{t+1} : U_I|_{t+1} \rightarrow \mathbb{R}^6$  - the derivative map defined in the image space;  
 $\mathcal{C}_I|_{t+1} : U_I|_{t+1} \rightarrow RGB$  - the texture map defined in the image space;  
 $\hat{\mathcal{P}}'_C|_{t+1} : \hat{U}'_C|_{t+1} \rightarrow \mathbb{R}^3$  - the reparamterized 3D point map defined in the canonical space;  
 $d\hat{\mathcal{P}}'_C|_{t+1} : \hat{U}'_C|_{t+1} \rightarrow \mathbb{R}^6$  - the reparameterized derivative map defined in the canonical space;  
 $\hat{\mathcal{C}}'_C|_{t+1} : \hat{U}'_C|_{t+1} \rightarrow RGB$  - the reparameterized texture map defined in the canonical space

**output**:  $\hat{\mathcal{P}}_C|_{t+1} : \hat{U}_C|_{t+1} \rightarrow \mathbb{R}^3$  - the fused 3D point map defined in the canonical space;  
 $d\hat{\mathcal{P}}_C|_{t+1} : \hat{U}_C|_{t+1} \rightarrow \mathbb{R}^6$  - the fused derivative map defined in the canonical space;  
 $\hat{\mathcal{C}}_C|_{t+1} : \hat{U}_C|_{t+1} \rightarrow RGB$  - the fused texture map defined in the canonical space

- 1 Fuse the parameter set  $\hat{U}_C|_{t+1} = \hat{U}'_C|_{t+1} \cup U_I|_{t+1}$ ;
- 2 Initialize  $\hat{\mathcal{P}}_C|_{t+1}$ ,  $d\hat{\mathcal{P}}_C|_{t+1}$  and  $\hat{\mathcal{C}}_C|_{t+1}$  ;
- 3 **for** each data point  $(u, v) \in U_C|_{t+1}$  **do**
- 4     **if** is texture map **then**
- 5         **if** there is data at data point  $(u, v)$  in the image space **then**
- 6             keep the data in the image space
- 7         **else**
- 8             keep the data in the canonical space
- 9         **end**
- 10     **else**
- 11         **if** there is data at data point  $(u, v)$  in the canonical space **then**
- 12             keep the data in the canonical space
- 13         **else**
- 14             keep the data in the image space
- 15         **end**
- 16     **end**
- 17 **end**

---

### 3.9. Surface strain estimation

In this section, we introduce how to leverage the recovered canonical maps to estimate tissue surface strain. We offer two ways to extract the strain data: the inter-frame strain and the accumulative strain.

*Inter-frame strain.* The inter-frame canonical local deformation map  $\mathcal{D}_C|_t$  is the optimization target as discussed previously. For each data point  $(u, v) \in U_C|_t$ , a deformation descriptor  $\mathbf{d}$  can be found as  $\mathbf{d} = \mathcal{D}_C|_t(u, v) \in \mathbb{D}$ .

$\mathbf{d}$  contains the stretch part, and it is trivial to turn stretch to strain. Therefore, the inter-frame strain can be obtained instantly from the recovered deformation map.

*Accumulative strain.* More often, we want to continuously track surface points and observe their accumulative strain. In this study, the tracking of 3D surface points is realized by tracking the 2D data points in the canonical space. One can easily calculate the inter-frame optical flow map  $\mathcal{O}_C|_t$  given the inter-frame displacement map  $\mathcal{F}_C|_t$  (Chen et al., 2024b). Let’s say we want to track the surface point from the  $n$ -th frame. To begin with, the canonical 3D point map at the  $n$ -th frame is  $\mathcal{P}_C|_n$ . By iteratively applying the inter-frame optical flow map, we can track the 2D data points continuously, as:

$$U_C|_{n \rightarrow n+m} = \mathcal{O}_C|_{n+m-1} \circ \dots \circ \mathcal{O}_C|_n(U_C|_n) \quad (7)$$

Accordingly, the tracked 3D points are  $\mathcal{P}_C|_{n+m}(\mathbf{p}), \mathbf{p} \in U_C|_{n \rightarrow n+m}$ . With the tracked point map, the accumulative deformation between the  $n$ -th frame and the  $(n+m)$ -th frame  $(\mathcal{F}_C|_{n \rightarrow n+m}, \mathcal{D}_C|_{n \rightarrow n+m})$  can be calculated according to section 3.2. The stretch part in  $\mathcal{D}_C|_{n \rightarrow n+m}$  can be easily extracted and converted to strain, which is now the accumulative one.

## 4. Experiment

### 4.1. Implementation details

The proposed method takes the 3D structure and 3D tracking as the inputs. In this study, the 3D structure is obtained by 3D reconstruction based on a stereo matching method, namely RAFT-Stereo (Lipson et al., 2021), and the 3D tracking is obtained in an approach (Chen et al., 2023) leveraging a 2D optical flow method, namely LiteFlowNet3 (Hui and Loy, 2020). We implement the method mainly using MATLAB<sup>®</sup> and CUDA<sup>®</sup> C++. The method can be run in an online approach with low GPU consumption as it doesn’t involve model training. We have tested on two platforms: *Platform 1* CPU AMD<sup>®</sup> 5800x with GPU NVIDIA<sup>®</sup> 3070, and *Platform 2* CPU Intel<sup>®</sup> 13900F with GPU NVIDIA<sup>®</sup> 3090ti. We jointly use MATLAB<sup>®</sup> and MeshLab (Cignoni et al., 2008) for visualization and rendering.

### 4.2. Datasets and evaluation metrics

We conducted the experiment using *in vivo* and *ex vivo* binocular laparoscopic datasets. All datasets are publicly available, namely HAMLYN (Mountney et al., 2010), ENDONERF (Wang et al., 2022), and SURGEM (Chen



et al., 2024a). Both HAMLYN and ENDONERF are *in vivo*, while SURGEM is *ex vivo*. The cameras in all these datasets were calibrated. The HAMLYN dataset we used involves large camera motion but mild tissue deformation. There is no instrument in the view, and no ground truth 3D structure is provided. ENDONERF involves tool-tissue interactions in the ways of dissection, grasping, and traction, where the camera is always fixed. Instrument masks are given to indicate the occluded area. No ground truth geometry is provided. SURGEM involves tool-tissue interaction in the way of palpation, where the camera is also fixed. Instrument masks and poses and ground truth 3D structures are provided. The ground truth 3D structures are acquired by 3D scanning from the back of thin tissue; thus, the structure in both the non-occluded and occluded areas is provided.

We evaluate the performance of the proposed method both quantitatively and qualitatively. Root mean square error (RMSE) and mean surface distance (MSD) (Chen et al., 2023) are used to quantify the 3D structure accuracy. The proposed method is compared to the previous tissue deformation recovery methods. Note that we only compare with those methods that have guaranteed geometric accuracy and are declared to be robust to occlusion for fairness, including EndoSurf (Zha et al., 2023) and TWPI (Chen et al., 2024b). The 3D reconstructed result obtained by RAFT-Stereo (Lipson et al., 2021) is used for reference, as it is used as the input of all the implemented methods, and RAFT-Stereo is not robust to occlusion.

## 5. Result and discussion

### 5.1. 3D reconstruction accuracy

Quantitative experiments on the SURGEM dataset (Chen et al., 2024a) were conducted to evaluate the 3D reconstruction accuracy of the deformable shape in both the non-occluded and the occluded areas. Results are shown in Table 2. All the methods involved in this experiment rely on the RAFT-Stereo result as their input, and thus, the RAFT-Stereo accuracy can be regarded as a reference. However, since RAFT-Stereo is not robust to occlusion, no information can be acquired in the occluded area. As can be seen from Table 2, the proposed method outperforms all methods in the non-occluded area and achieves similar performance in the occluded area as compared to our previous work (Chen et al., 2024b). In the case when instrument pose information is available, the proposed method shows the highest accuracy in both the non-occluded and the occluded areas. In the

case when tool-induced occlusion occurs but instrument pose information is unavailable, the accuracy of the proposed method drops in the occluded area. Besides, we want to highlight that the proposed method, as an online method, outperforms EndoSurf (Zha et al., 2023), which is offline, showing promising potential for intraoperative applications.

Table 2: Deformation recovery accuracy on the SURGEM dataset (unit in millimeter)

Methods	Non-occluded		Occluded	
	RMSE ( $\downarrow$ )	MSD $\pm$ std ( $\downarrow$ )	RMSE ( $\downarrow$ )	MSD $\pm$ std ( $\downarrow$ )
RAFT-Stereo (Lipson et al., 2021)	0.50	$0.39 \pm 0.32$	n.a.	n.a.
EndoSurf (Zha et al., 2023)	3.52	$2.26 \pm 2.71$	8.75	$8.19 \pm 3.10$
TWPI (Chen et al., 2024b) w/o pose	1.18	$0.79 \pm 0.88$	3.53	$2.98 \pm 1.89$
TWPI (Chen et al., 2024b) w/ pose	0.90	$0.63 \pm 0.63$	0.48	$0.40 \pm 0.26$
Proposed w/o pose	0.82	$0.51 \pm 0.64$	3.70	$3.16 \pm 1.94$
Proposed w/ pose	0.45	$0.37 \pm 0.27$	0.44	$0.39 \pm 0.21$

**Abbreviations** RMSE: root mean square error; MSD $\pm$ std: mean surface distance  $\pm$  standard deviation; Non-occluded/Occluded: surface accuracy in the non-occluded and the occluded areas; w/ pose: instrument pose-constrained optimization; w/o pose: optimization without instrument pose priors.

### 5.2. Camera-pose-free performance

In this section, we want to prove that even as a totally camera-pose-free approach, the proposed method can still handle camera motion without significant coordinate drift. The experiment was conducted on the HAMLIN dataset (Mountney et al., 2010), where the camera is viewing around the abdominal wall and tissue deformation is mild. To compare with the camera-pose-based approach, we first estimate the camera pose using ORB-SLAM2 (Mur-Artal and Tardós, 2017) implemented by MATLAB<sup>®</sup>. Though ORB-SLAM2 is not designed for a deformable scene, it can still roughly estimate the camera pose given mild deformation. After that, points reconstructed from different frames are aligned together to the final camera coordinate. In Fig. 7, we visualize the aligned points and the recovered surface by the proposed method together for qualitative comparison. As can be seen in Fig. 7, the aligned points diffuse in the space, while the recovered surface does not. Although the deformation is mild, the lowly textured tissue surface also hinders accurate camera pose estimation, which relies on key feature

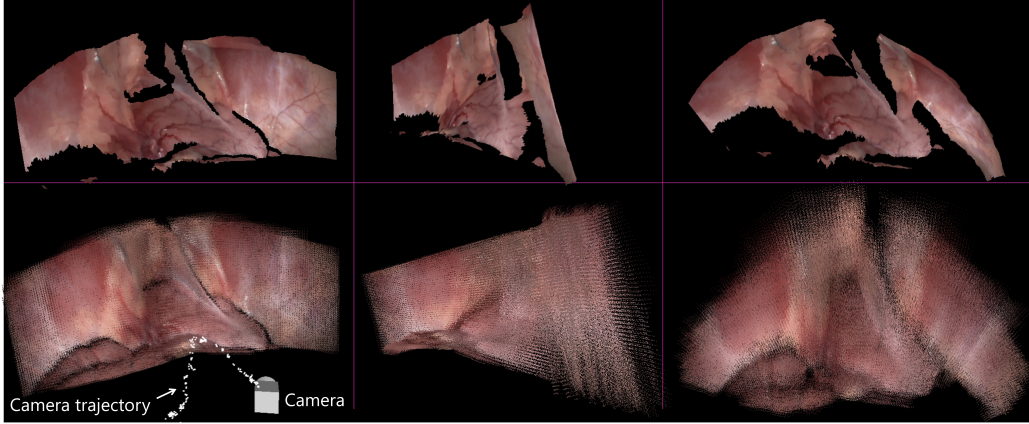


Figure 7: The reconstructed tissue structure with texture in the last frame. The results of the proposed method (top row) and of the camera-based approach (bottom row) are visualized together for comparison (observed from the same view angle with the same scaling). The left, middle, right columns show the front, side, top views, respectively.

point matching. We can also see that the shape of the recovered surface fits well with the distribution of the diffused aligned points, demonstrating that the proposed camera-pose-free can indeed guarantee meaningful inter-frame alignment without significant coordinate drift. This makes us believe that camera pose may not be necessary for the reconstruction of dynamic scenes under the assumption that part of the visible tissue is always connected to the invisible one.

### 5.3. Deformation recovery and surface strain estimation in various surgical manipulation

This section presents the recovery results of tissue deformation in various surgical manipulations, including camera motion, traction, dissection, and palpation. In addition, the results of the surface strain estimation are also presented in the cases of traction and palpation, where the tissue deformation is continuous and significant.

Fig. 8 shows the online behavior of the proposed method. The method gradually recovers the structure of a deformable scene. The structure that is initially occluded by the instrument or is outside the field of view will be added once it becomes visible. On the other hand, if the structure used to be observable but is currently occluded or outside the field of view, it will still be maintained in the recovered results, proving that the proposed method is

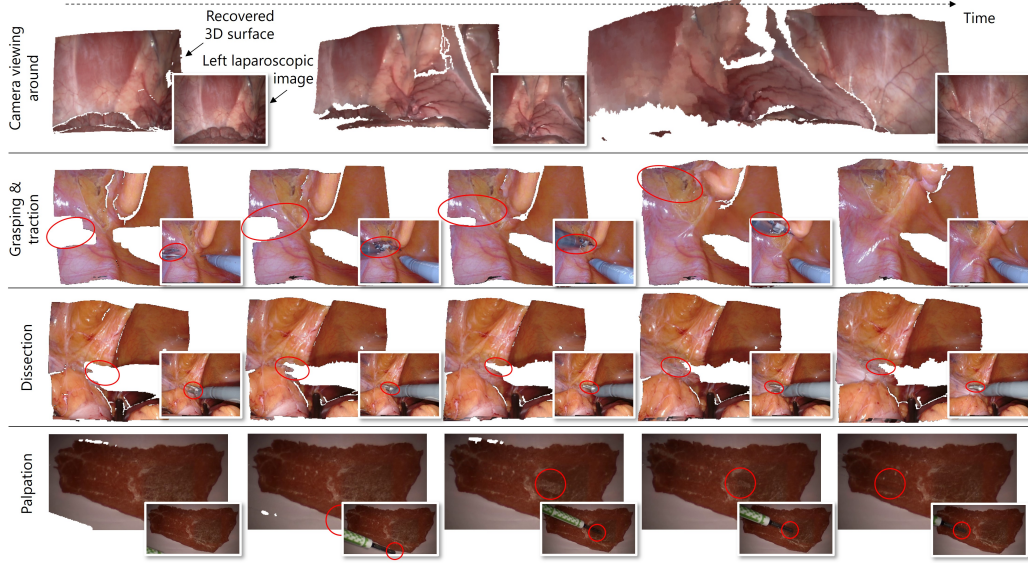


Figure 8: Results of the proposed online deformation recovery method together with the corresponding laparoscopic image frames. Time increases from the left to the right. Red rings indicate the locations of the instrument tip. In the first row, the camera is moving around viewing the abdominal wall, but the tissue deformation is mild. In the second row, two forceps cause severe occlusion. One forceps perform grasping and traction, while the other is idle. In the third row, one forceps is performing dissection, leading to the change in tissue surface continuity. In the fourth row, one forceps approach and push the tissue surface, and then leave.

robust to occlusion and camera motion. When the geometric continuity of the tissue changes in the case of dissection, the proposed method can model the newly exposed surface and update the geometry and texture to make it consistent with the latest observation. However, the proposed method does not tend to recover the permanently invisible structure, leaving some vacant regions, as can be seen in Fig. 8.

Fig. 9 shows the estimated surface strain overlaid on the recovered tissue structure, together with the corresponding laparoscopic frame image. We want to clarify that the surface strain visualized in Fig. 9 is the maximal principal inner-surface small strain. In our previous method (Chen et al., 2024b), surface strain estimation is not convenient since only the displacement map is modeled, while the proposed method directly models the stretching effect in the deformation map, from which surface strain can be easily obtained. We manually select the region of interest to continuously track surface points

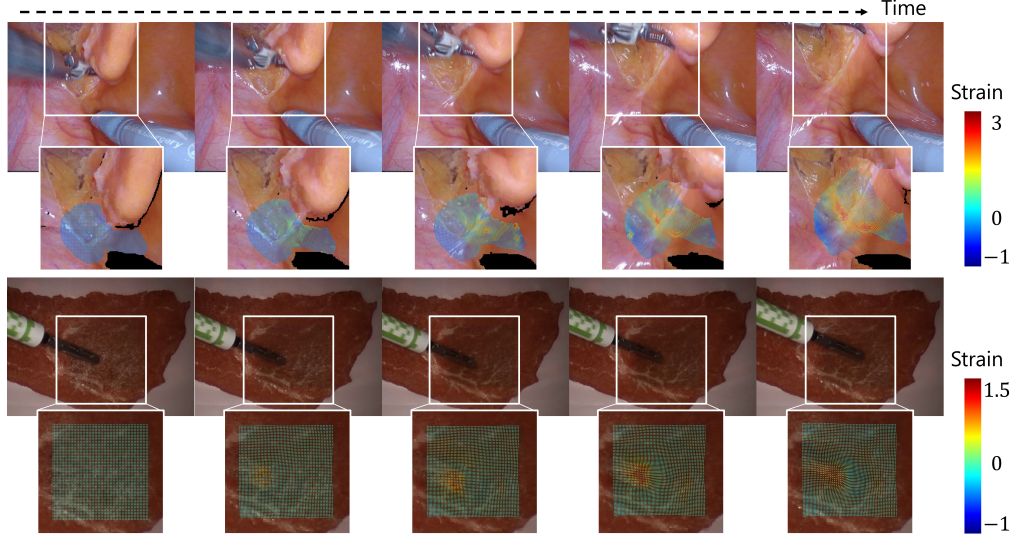


Figure 9: The estimated surface maximal strain using the proposed method. Time increases from the left to the right. The first and the third rows are the images from the laparoscopic camera. The second and the fourth rows are the colored maximal surface principal strain overlaid with the recovered tissue surface. The first and the second rows show the case in traction, where the tissue surface is stretched. The third and the fourth rows show the case in palpation, where the forceps approach, push, and leave the tissue.

and measure the strain, as shown in Fig. 9. The surface strain is initially zero and gradually increases when tissue deformation becomes severe. The surface strain distribution is inhomogeneous as the deformation is non-affine. In the case of traction, the maximal strain occurs around the center line of the stretched surface, while in the case of palpation, the maximal strain occurs around the forceps tip. Results show that the proposed method can estimate surface strain under different manipulations with robustness to occlusion, and that the laparoscopic image-derived surface strain may be a new and useful modality for tool-tissue interaction analysis.

#### 5.4. Runtime performance

As an online method, we evaluate the runtime performance of the proposed method by modifying the number of data points and measuring the time per iteration. Note that only the time for deformation optimization is counted, while the time for measurement and data input/output (I/O) is ignored. Given an image with the resolution of  $W \times H$ , if there is no

downsampling or compressing process, the initial number of data points will be the same as that of the pixels and will gradually increase if the field of view changes. Take an image in the SURGEM dataset as an example; it has the resolution of  $1280 \times 720$ , resulting in the initial number of data points of 921600 and around 800000 after outlier detection. It takes about 9.96 seconds for an iteration on *Platform 1* and 6.28 seconds on *Platform 2*, as shown in Fig. 10. If we downsample the data points from 800000 to 30000, the time per iteration drops to 0.25 second on *Platform 1* and 0.20 second on *Platform 2*. As shown in Fig. 10, the time per iteration is almost proportional to the number of data points. We believe that the current bottleneck of the runtime performance is in the CPU side, as the solver of the optimization problem is working on CPU only, and the GPU consumption is always low (less than 10%) during the optimization.

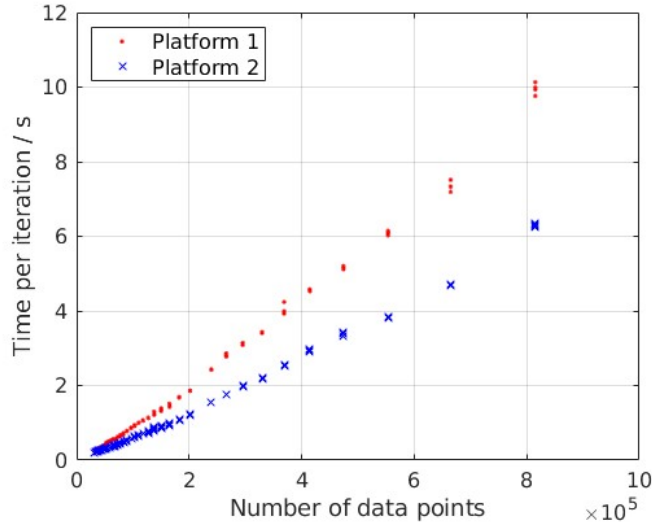


Figure 10: Runtime performance of the proposed method. *Platform 1*: CPU AMD<sup>®</sup> 5800x with GPU NVIDIA<sup>®</sup> 3070. *Platform 2*: CPU Intel<sup>®</sup> 13900F with GPU NVIDIA<sup>®</sup> 3090ti.

### 5.5. Limitation and future work

Though continuous deformable scene reconstruction when the camera is moving has been demonstrated in section 5.2, the proposed method does not optimize the stretching effect for those geometries outside the field of

view. Instead, only the 3D position and orientation of these geometries are optimized. In other words, the geometry outside the field of view is regarded as a rigid body connecting with the deformable geometry inside the field of view. The biomechanical property and boundary condition of some of the invisible tissue may be different from those of the visible one, making it less reliable to estimate the deformation of the invisible tissue that locates far away from the visible one. Moreover, projection-based parameterization is implemented in this article, which cannot model self-folding geometry nor the geometry at the backside of the camera.

Since the proposed method only utilizes inter-frame data for optimization and fusion, long-term stability is not guaranteed. Misalignment may occur during a revisit, and the current method simply replaces the historical data with the latest one. However, smoothing using historical data based on concepts like bundle adjustment (Guo and Gallego, 2024) may help to improve the long-term stability of frame alignment. Additionally, as a camera-pose-free approach, the proposed method aligns frame data based on the assumption of tissue connectivity. Therefore, when the tissue connection becomes weak, the estimation becomes unstable.

Realtime performance is another concern when trying to yield an method for intraoperative application. The proposed method has online behavior, but we still carefully choose to not use the word “realtime” at the current stage. Although in the experiment we can see that the processing time of per-frame data can be lower than 0.2 second, this does not count the time for acquiring the initial depth and optical flow data, which varies depending on the exact method in use and the data resolution. Besides the data acquisition time, the current bottleneck remains in the CPU code for solving the constrained linear programming problem.

## 6. Conclusion

This article presents a vision-based method for continuous tissue deformation recovery. The method works in an online approach and optimizes inter-frame tissue geometry and deformation using only the current and the previous frame data. Tissue geometry is represented by the 3D point map and derivative map, while tissue deformation is represented by the 3D displacement map and local deformation map. Inter-frame alignment is realized via optimizing the inter-frame deformation, and thus, camera pose is unnecessary. With the tissue-invariant vision-biomechanics consistency constraints,

the proposed method can be adapted to various tissues under various surgical manipulations. Quantitative and qualitative experiments were conducted on the *in vivo* and *ex vivo* laparoscopic datasets. Results prove that the proposed method is robust to tool-induced occlusion, can handle camera motion, and always keeps consistency with the latest observation even when new tissue surfaces occur. The proposed method achieves the highest reconstruction accuracy with errors in the non-occluded area as  $0.37 \pm 0.27$  mm and in the occluded area as  $0.39 \pm 0.21$  mm. The proposed method also helps to quantify the surface strain during palpation and traction, where the surface strain may be used as a new modality for tool-tissue interaction analysis, risk assessment, and surgical task automation.

### Declaration of competing interest

The authors declare that they have no known competing financial interests or personal relationships that could have appeared to influence the work reported in this paper.

### Acknowledgments

This research is supported by JST Moonshot R&D Grant (Number JP-MJMS2214 - 02) and the Grand-in-Aid for JSPS Fellows (Number 25KJ1017).

### References

- Bardozzo, F., Collins, T., Forgione, A., Hostettler, A., Tagliaferri, R., 2022. StaSiS-Net: A stacked and siamese disparity estimation network for depth reconstruction in modern 3D laparoscopy. *Med. Image Anal.* 77, 102380.
- Budd, C., Vercauteren, T., 2024. Transferring relative monocular depth to surgical vision with temporal consistency, in: *Medical image computing and computer assisted intervention – MICCAI 2024*, pp. 692–702.
- do Carmo, M., 2016. *Differential Geometry of Curves and Surfaces: Revised and Updated Second Edition*. Dover Books on Mathematics, Dover Publications.
- Chavarrias Solano, P.E., Bulpitt, A., Subramanian, V., Ali, S., 2025. Multi-task learning with cross-task consistency for improved depth estimation in colonoscopy. *Med. Image Anal.* 99, 103379.



- Chen, J., Hara, K., Kobayashi, E., Sakuma, I., Tomii, N., 2023. Occlusion-robust scene flow-based tissue deformation recovery incorporating a mesh optimization model. *Int. J. Comput. Assist. Radiol. Surg.* 18, 1043–1051.
- Chen, J., Kobayashi, E., Sakuma, I., Tomii, N., 2024a. Surgem: A vision-based surgery environment modeling framework for constructing a digital twin toward autonomous soft tissue manipulation. *IEEE Robot. Autom. Lett.* 9, 9789–9796.
- Chen, J., Kobayashi, E., Sakuma, I., Tomii, N., 2024b. Trans-window panoramic impasto for online tissue deformation recovery, in: *Medical image computing and computer assisted intervention – MICCAI 2024*, pp. 681–691.
- Chen, L., Tang, W., John, N.W., Wan, T.R., Zhang, J.J., 2018. SLAM-based dense surface reconstruction in monocular minimally invasive surgery and its application to augmented reality. *Comput. Methods Programs Biomed.* 158, 135–146.
- Cignoni, P., Callieri, M., Corsini, M., Dellepiane, M., Ganovelli, F., Ranzuglia, G., 2008. MeshLab: An open-source mesh processing tool, in: *Sixth eurographics italian chapter conference*, pp. 129–136.
- Giannarou, S., Ye, M., Gras, G., Leibbrandt, K., Marcus, H.J., Yang, G.Z., 2016. Vision-based deformation recovery for intraoperative force estimation of tool–tissue interaction for neurosurgery. *Int. J. Comput. Assist. Radiol. Surg.* 11, 929–936.
- Guo, J., Wang, J., Kang, D., Dong, W., Wang, W., Liu, Y.h., 2024. Free-SurGS: SfM-free 3D gaussian splatting for surgical scene reconstruction, in: *Medical image computing and computer assisted intervention – MICCAI 2024*, pp. 350–360.
- Guo, S., Gallego, G., 2024. Cmax-slam: Event-based rotational-motion bundle adjustment and slam system using contrast maximization. *IEEE Trans. Robot.* 40, 2442–2461.
- Gómez-Rodríguez, J.J., Lamarca, J., Morlana, J., Tardós, J.D., Montiel, J.M.M., 2021. SD-DefSLAM: Semi-direct monocular SLAM for deformable and intracorporeal scenes, in: *2021 IEEE international conference on robotics and automation (ICRA)*, pp. 5170–5177.

- Haouchine, N., Dequidt, J., Berger, M.O., Cotin, S., 2015. Monocular 3D reconstruction and augmentation of elastic surfaces with self-occlusion handling. *IEEE Trans. Vis. Comput. Graph.* 21, 1363–1376.
- Haouchine, N., Kuang, W., Cotin, S., Yip, M., 2018. Vision-based force feedback estimation for robot-assisted surgery using instrument-constrained biomechanical three-dimensional maps. *IEEE Robot. Autom. Lett.* 3, 2160–2165.
- Hayoz, M., Hahne, C., Gallardo, M., Candinas, D., Kurmann, T., Allan, M., Sznitman, R., 2023. Learning how to robustly estimate camera pose in endoscopic videos. *Int. J. Comput. Assist. Radiol. Surg.* 18, 1185–1192.
- Hu, J., Jones, D., Dogar, M.R., Valdastrì, P., 2024. Occlusion-robust autonomous robotic manipulation of human soft tissues with 3-D surface feedback. *IEEE Trans. Robot.* 40, 624–638.
- Hui, T.W., Loy, C.C., 2020. LiteFlowNet3: Resolving correspondence ambiguity for more accurate optical flow estimation, in: *Computer vision – ECCV 2020*, pp. 169–184.
- Lamarca, J., Parashar, S., Bartoli, A., Montiel, J.M.M., 2021. DefSLAM: Tracking and mapping of deforming scenes from monocular sequences. *IEEE Trans. Robot.* 37, 291–303.
- Li, Y., Richter, F., Lu, J., Funk, E.K., Orosco, R.K., Zhu, J., Yip, M.C., 2020. SuPer: A surgical perception framework for endoscopic tissue manipulation with surgical robotics. *IEEE Robot. Autom. Lett.* 5, 2294–2301.
- Liang, X., Liu, F., Zhang, Y., Li, Y., Lin, S., Yip, M., 2024. Real-to-sim deformable object manipulation: Optimizing physics models with residual mappings for robotic surgery, in: *2024 IEEE international conference on robotics and automation (ICRA)*, pp. 15471–15477.
- Lipson, L., Teed, Z., Deng, J., 2021. RAFT-Stereo: Multilevel recurrent field transforms for stereo matching, in: *2021 International Conference on 3D Vision (3DV)*, pp. 218–227.
- Luo, X., Xie, L., Zeng, H.Q., Wang, X., Li, S., 2023. Monocular endoscope 6-DoF tracking with constrained evolutionary stochastic filtering. *Med. Image Anal.* 89, 102928.

- Mountney, P., Stoyanov, D., Yang, G.Z., 2010. Three-dimensional tissue deformation recovery and tracking. *IEEE Signal Process. Mag.* 27, 14–24.
- Mur-Artal, R., Tardós, J.D., 2017. ORB-SLAM2: An open-source SLAM system for monocular, stereo, and RGB-D cameras. *IEEE Trans. Robot.* 33, 1255–1262.
- Ozyoruk, K.B., Gokceler, G.I., Bobrow, T.L., Coskun, G., Incetan, K., Almalioglu, Y., Mahmood, F., Curto, E., Perdigoto, L., Oliveira, M., Sahin, H., Araujo, H., Alexandrino, H., Durr, N.J., Gilbert, H.B., Turan, M., 2021. EndoSLAM dataset and an unsupervised monocular visual odometry and depth estimation approach for endoscopic videos. *Med. Image Anal.* 71, 102058.
- Psychogios, D., Mazomenos, E., Vasconcelos, F., Stoyanov, D., 2022. MS-DESI: Multitask stereo disparity estimation and surgical instrument segmentation. *IEEE Trans. Med. Imaging* 41, 3218–3230.
- Pumarola, A., Corona, E., Pons-Moll, G., Moreno-Noguer, F., 2021. D-Nerf: Neural radiance fields for dynamic scenes, in: 2021 IEEE/CVF conference on computer vision and pattern recognition (CVPR), pp. 10313–10322.
- Recasens, D., Lamarca, J., Facil, J.M., Montiel, J.M.M., Civera, J., 2021. Endo-Depth-and-Motion: Reconstruction and tracking in endoscopic videos using depth networks and photometric constraints. *IEEE Robot. Autom. Lett.* 6, 7225–7232.
- Scheikl, P.M., Tagliabue, E., Gyenes, B., Wagner, M., Dall’Alba, D., Fiorini, P., Mathis-Ullrich, F., 2023. Sim-to-real transfer for visual reinforcement learning of deformable object manipulation for robot-assisted surgery. *IEEE Robot. Autom. Lett.* 8, 560–567.
- Schmidt, A., Mohareri, O., DiMaio, S., Yip, M.C., Salcudean, S.E., 2024. Tracking and mapping in medical computer vision: A review. *Med. Image Anal.* 94, 103131.
- Schneider, C., Allam, M., Stoyanov, D., Hawkes, D.J., Gurusamy, K., Davidson, B.R., 2021. Performance of image guided navigation in laparoscopic liver surgery – A systematic review. *Surg. Oncol.* 38, 101637.

- Schonberger, J.L., Frahm, J.M., 2016. Structure-from-motion revisited, in: 2016 IEEE conference on computer vision and pattern recognition (CVPR), pp. 4104–4113.
- Shan, J., Li, Y., Xie, T., Wang, H., 2024. ENeRF-SLAM: A dense endoscopic SLAM with neural implicit representation. *IEEE Trans. Med. Robot. Bionics* 6, 1030–1041.
- Shao, S., Pei, Z., Chen, W., Zhu, W., Wu, X., Sun, D., Zhang, B., 2022. Self-supervised monocular depth and ego-motion estimation in endoscopy: Appearance flow to the rescue. *Med. Image Anal.* 77, 102338.
- Spencer, A., 2004. *Continuum Mechanics*. Dover books on physics, Dover Publications.
- Stoyanov, D., 2012. Stereoscopic scene flow for robotic assisted minimally invasive surgery, in: *Medical image computing and computer-assisted intervention – MICCAI 2012*, pp. 479–486.
- Wang, Q., Zhao, S., Xu, Z., Zhou, S.K., 2025. LACOSTE: Exploiting stereo and temporal contexts for surgical instrument segmentation. *Med. Image Anal.* 99, 103387.
- Wang, Y., Long, Y., Fan, S.H., Dou, Q., 2022. Neural rendering for stereo 3D reconstruction of deformable tissues in robotic surgery, in: *Medical image computing and computer assisted intervention – MICCAI 2022*, pp. 431–441.
- Wei, R., Li, B., Chen, K., Ma, Y., Liu, Y., Dou, Q., 2024. Enhanced scale-aware depth estimation for monocular endoscopic scenes with geometric modeling, in: *Medical image computing and computer assisted intervention – MICCAI 2024*, pp. 263–273.
- Widya, A.R., Monno, Y., Imahori, K., Okutomi, M., Suzuki, S., Gotoda, T., Miki, K., 2019. 3D reconstruction of whole stomach from endoscope video using structure-from-motion, in: *2019 41st annual international conference of the IEEE engineering in medicine and biology society (EMBC)*, pp. 3900–3904.

- Xia, W., Chen, E.C.S., Pautler, S., Peters, T.M., 2022. A robust edge-preserving stereo matching method for laparoscopic images. *IEEE Trans. Med. Imaging* 41, 1651–1664.
- Xu, T., Lei, Y., Cheng, X., Li, M., 2022. Identification of Young’s modulus and equivalent spring constraint boundary conditions of the soft tissue with locally observed displacements for endoscopic liver surgery. *Comput. Methods Biomech. Biomed. Eng.* 25, 439–454.
- Yamamoto, K., Hara, K., Kobayashi, E., Yuki, A., Sakuma, I., 2023. Tissue histology on the correlation between fracture energy and elasticity. *Int. J. Comput. Assist. Radiol. Surg.* .
- Yang, S., Li, Q., Shen, D., Gong, B., Dou, Q., Jin, Y., 2024. Deform3DGS: Flexible deformation for fast surgical scene reconstruction with gaussian splatting, in: *Medical image computing and computer assisted intervention – MICCAI 2024*, pp. 132–142.
- Yoshimura, M., Marinho, M.M., Harada, K., Mitsuishi, M., 2021. MBAPose: Mask and bounding-box aware pose estimation of surgical instruments with photorealistic domain randomization, in: *2021 IEEE/RSJ international conference on intelligent robots and systems (IROS)*, pp. 9445–9452.
- Zha, R., Cheng, X., Li, H., Harandi, M., Ge, Z., 2023. EndoSurf: Neural surface reconstruction of deformable tissues with stereo endoscope videos, in: *Medical image computing and computer assisted intervention – MICCAI 2023*, pp. 13–23.
- Zhang, C., Liu, Y., Wang, K., Tian, J., 2023. Specular highlight removal for endoscopic images using partial attention network. *Phys. Med. Biol.* 68, 225009.
- Zhu, J., Su, Y., Liu, Z., Liu, B., Sun, Y., Gao, W., Fu, Y., 2022. Real-time biomechanical modelling of the liver using LightGBM model. *Int. J. Med. Robot. Comput. Assist. Surg.* 18, e2433.